Article

Tuned S-Scheme Cu₂S_TiO₂_WO₃ Heterostructure Photocatalyst toward S-Metolachlor (S-MCh) Herbicide Removal

Alexandru Enesca [1,*] and Luminita Isac [2]

[1] Product Design, Mechatronics and Environmental Department, Transilvania University of Brasov, 35000 Brasov, Romania

[2] Renewable Energy Systems and Recycling Research Center, Transilvania University of Brasov, Eroilor 29 Street, 35000 Brasov, Romania; isac.luminita@unitbv.ro

[*] Correspondence: aenesca@unitbv.ro

Abstract: A dual S-scheme Cu₂S_TiO₂_WO₃ heterostructure was constructed by sol–gel method using a two-step procedure. Due to the synthesis parameters and annealing treatment the heterostructure is characterized by sulfur deficit and oxygen excess allowing the passivation of oxygen vacancies. The photocatalytic activity was evaluated under UV and UV–Vis irradiation scenarios using S-MCh as reference pollutant. The heterostructure is composed on orthorhombic Cu₂S, anatase TiO₂ and monoclinic WO₃ with crystallite sizes varying from 65.2 Å for Cu₂S to 97.1 Å for WO₃. The heterostructure exhibit a dense morphology with pellets and particle-like morphology closely combined in a relatively compact assembly. The surface elemental composition indicate that the heterostructure maintain a similar atomic ratio as established during the synthesis with a slight sulfur deficit due to the annealing treatments. The results indicate that the three-component heterostructure have higher photocatalytic efficiency (61%) comparing with two-component heterostructure or bare components. Moreover, Cu₂S_TiO₂_WO₃ exhibit a superior constant rate (0.114 s^{-1}) due to the high concentration of photogenerated charge carriers, efficient charge separation and migration.

Keywords: herbicide; s-metolachlor; wastewater; photocatalysis; semiconductors; S-scheme mechanism

1. Introduction

Aquatic contamination with recalcitrant organic compounds released by industrial, agricultural, and transportation activities represent a serious threat to human health and life quality. Pesticide compounds including herbicides, insecticides, and fungicides have large contamination potential due to their continuous use in agricultural area and long term persistency in the ecological system [1–3]. The agricultural accumulation of organic compounds, such as S-metolachlor, cyprodinil, iprodione, tebuconazole, etc., in sediment and biota, are sources of serious environmental pollution [4,5]. Finding new and sustainable pathways for water decontamination represent an important target for the future of agriculture and wastewater plants. Photocatalytic technologies use the light energy as driving force to induce organic pollutant oxidation. The use of mono-component photocatalysts such as TiO₂ [6], WO₃ [7], SnO₂ [8], Cu₂S [9], CuO [10], or NiO [11] presents several disadvantages: (i) limited light absorption range, (ii) fast charge carriers recombination, and (iii) reduced chemical stability.

The photocatalytic process is based on three major steps: (1) the electron/hole pairs formation during irradiation due to the semiconductors absorption of photons with energy (hv) equal to or above their bandgap (Eg); (2) the separation and diffusion of photogenerated carriers under the action of the internal electric field; (3) formation of oxidative and super-oxidative species due to the surfaces reactions induced by the photogenerated electrons and holes [12–14]. TiO₂ and WO₃ have band gap values of 3.2 eV and 2.8 eV, which means that they are mostly active in the UV spectra. The charge carriers are photogenerated when the photons energy are equal or higher than the band gap value. Cu₂S is

photoactivated in Vis spectra due to his band gap value which may vary between 1.2 eV and 2.0 eV, depending on the stoichiometric composition. When coupled, the band gap values shift in order to generate a build in electric field required for charge carriers mobility through the heterostructure. Traditional heterojunctions (such as type-II heterojunctions, p-n junction) typically produce unfavorable losses of the photogenerated charges, while the Z-scheme heterostructure represent the starting point on the development of S-scheme heterostructure [15,16]. If compared with Z-scheme heterostructure, the S-scheme efficiently use the build-in electric field in order to reduce the migration distance of photogenerated electrons and holes based on the synergetic interface between the semiconductor components [17,18].

The S-scheme heterostructure consists of two or more semiconductors with suitable position of the energy bands. The driving force responsible of the charge migration is represented by the internal electric field established between the heterostructure components [19,20]. The photogenerated charges are separated in space, based on the semiconductors potential: the holes are located in the conduction band (CB) of the reduction photocatalyst and the electrons are in the valence band (VB) of the oxidation photocatalyst, respectively [21,22]. The photocatalytic reactions generating the (super)oxidative ($\bullet OH$, $\bullet O_2^-$) species are initiated by the photogenerated holes and electrons. Therefore, efficient S-scheme heterostructure is highly desirable, in order to promote the charge migration and to sustain favorable charge potentials [23,24]. Until now, several S-scheme heterostructures such as $SnFe_2O_4/ZnFe_2O_4$ [25], $TiO_2/W_{18}O_{49}$ [26], $NiO/BiOI$ [27], $BiVO_4@MoS_2$ [28], $WO_3/CdIn_2S_4$ [29], $CdS/UiO-66$ [30] were tested for dyes or pharmaceutical active compounds removal. The $SnFe_2O_4/ZnFe_2O_4$ show enhanced Vis light absorbance and direct S-scheme path of charge separation and transfer. After 60 min of 300 W Vis light irradiation the $NiO/BiOI$ exhibited 90% Rhodamine B photocatalytic removal.

Herein, we report for the first time the photocatalytic removal of S-MCh herbicide using a dual S-scheme heterostructure and two irradiation scenarios. The composition and morphology was investigated and correlated with the photocatalytic properties and energy band diagram. The dual S-scheme mechanism facilitates the photogenerated charge carriers migration and the efficient use of redox potential to induce pollutant degradation. Compared with Z-scheme mechanism, the S-scheme heterostructure use the build-in electric field to mitigate the charge transmission distance due to the synergic semiconductors interface. The S-scheme mechanism is able to use more efficiently the photogenerated charge carriers based on the charge density difference between the heterostructure components. The kinetic evaluation indicates a higher oxidation reaction rate for the three-component heterostructure compared with two-components or single component photocatalysts.

2. Materials and Methods

2.1. Photocatalyst Materials

2.1.1. Preparation of Mono-Component Photocatalysts

Two powder components were prepared using sol–gel technique:

(i) Cu_2S was prepared by mixing 0.2 mol of copper nitrate ($Cu(NO_3)_2$, 99.9%, Scharlau, Barcelona, Spain) aqueous solution with 0.5 mol of sodium thiosulfate ($Na_2S_2O_3$, 99.9%, Scharlau) aqueous solution. After 15 min of stirring the gel was formed and kept 3 h undisturbed to achieve the complete precipitation. The precipitate was centrifuged and thermally treated at 120 °C in a ceramic capsule in sulfured (Sulfur, 99%, Sigma Aldrich, Munich, Germany) atmosphere.

(ii) WO_3 was obtained by dissolving tungsten hexachloride (WCl_6, 99.4%, Acros Organics, Geel, Belgium) in a mixture of ethanol (100%, Sigma Aldrich) and 2-propanol (100%, Sigma Aldrich). After 120 min of stirring a light yellow alcoholic solution was obtained. Then, 0.15 mol of natrium hydroxide (99.98%, Honeywell, Charlotte, NC, USA) was added drop by drop and the gel was formed. After precipitation and centrifugation the resulting powder was annealed for 8 h at 500 °C.

The TiO$_2$ powder was purchased (99.99%, Scharlau, Barcelona, Spain) and used without any purification procedures.

2.1.2. Preparation of Multi-Component Photocatalysts

Three bi-component and one three-component heterostructures were prepared by sol–gel technique:

(i) Cu$_2$S_TiO$_2$ sample was obtained using the same procedure as described for Cu$_2$S, with the single modification that TiO$_2$ powder was dispersed into copper nitrate solution, considering the Cu:Ti atomic ratio of 1:1. The final powder was thermally treated at 150 °C for 2 h.

(ii) Cu$_2$S_WO$_3$ sample was obtained following the procedure described for Cu$_2$S. The WO$_3$ powder already prepared was added into copper nitrate solution, considering the Cu:W atomic ratio of 1:1. The final powder was thermally treated at 150 °C for 1.5 h.

(iii) TiO$_2$_WO$_3$ sample was prepared as using a similar procedure as presented for WO$_3$, and the TiO$_2$ power was dispersed into tungsten hexachloride solution. The uniform TiO$_2$ distribution was assured by adding polyethylene glycol (99%, Scharlau) and the Ti:W atomic ratio was 1:1. The annealing treatment was done at 500 °C for 5 h.

(iv) Cu$_2$S_TiO$_2$_WO$_3$ sample was synthesized by adding TiO$_2$_WO$_3$ powder, previously obtained, into copper nitrate solution and the mixture was stirred for 2 h. The Cu:Ti:W atomic ratio was 1:1:1. Then, 0.7 mol of sodium thiosulfate (Na$_2$S$_2$O$_3$, 99.9%, Scharlau) was added drop by drop under continuous stirring. The precipitate was centrifuged and thermally treated at 150 °C for 2 h.

2.2. Photocatalytic Activity

The photocatalytic activity was tested using a closed reactor able to produce light irradiation from the top and lateral sides, which increase the radiation uniformity during the experiments. The reactor chamber use ventilation engines and thermocouples in order to preserve constant temperature (25 °C) and humidity (60%). Two kind of radiation sources were used (single or combined): 18W UVa black tubes (T8, 3Lx flux intensity, $\lambda_{\text{UVa,max}}$ = 365 nm, range 310–390 nm, Philips) and 18W Vis cold tubes (TL-D Super 80/865, flux intensity 28Lx, $\lambda_{\text{Vis,max}}$ = 565 nm, range 400–700 nm, Philips). Two irradiation scenarios where verified and the corresponding total irradiance is presented in Table 1.

Table 1. Irradiation scenarios for the photocatalytic applications.

Irradiation Sources	UV Radiation Sources (310–390 Nm)	Vis Radiation Sources (400–800 Nm)	Total Irradiance (W/M^2)
UVa light, 18 W	8	0	16.3
UVa–Vis light, 18 W	4	4	24.9

S-Metholachlor (S-MCh) herbicide was used as reference pollutant molecule, due to his reluctance to traditional wastewater treatments procedures as well as his toxicity and accumulation potential into the biota. High concentrations of S-MCh may induce cytotoxicity and genotoxicity effect localized in human lymphocytes. The photocatalytic experiments were done using 30 mg/L S-MCh aqueous solution and the photocatalyst dosage was 30 mg/50 mL. Quart recipients were considered due to high UV transmittance. The total time of experiment was 10 h: 2 h in dark to reach the absorption equilibrium and 8 h under irradiation. The pollutant concentration was measured hourly and compared with the UV–Vis is calibration curve (274 nm is the S-MCh absorption wavelength). Finally, the photocatalytic efficiency was calculated considering the initial (C_0) and final (C) concentrations based on the following Equation (1):

$$\eta = \left[\frac{(C_0 - C)}{C_0} \right] \cdot 100 \qquad (1)$$

2.3. Characterization Instruments

The presence of crystalline structure was evaluated using X-ray diffraction (XRD, Bruker, Model D8 Discover, Karlsruhe, Germany) with 0.003 degree scan step locked-couple technique and 0.015 s/step. The morphology characterizations were done with scanning electron microscopy (SEM, Hitachi model S–3400 N type 121 II, Tokyo, Japan) in high vacuum regime for mono-component samples and with field emission scanning electron microscopy (FESEM, SU8010, Fukuoka, Japan) operated at an accelerated voltage of 25 kV for multi-component samples. The light intensity and total irradiance values inside the photoreactor were measured using a class A high precision pyranometer (SR11, Hukselflux, Berlin, Germany). The optical properties as well as the photocatalytic activity were investigated using UV–Vis spectrometry (Perkin Elmer Lambda 950, Waltham, MA, USA).

3. Results and Discussions

3.1. Composition and Morphology

The evaluation of crystalline structure presented in Figure 1 indicates that TiO_2 has maintained the anatase structure (ICCD 83-0951) and crystallites size (Table 2), as received from the manufacturer, regardless the chemical and thermal treatments followed during the heterostructures development. The crystallite sizes were calculated based on the Scherrer formula, Equation (2):

$$D = \frac{0.9\lambda}{\beta \cos\theta} \tag{2}$$

where β is the observed angular width at half maximum intensity (FWHM) of the peak, λ is the X-ray wavelength (1.5406 Å for $CuK\alpha 1$), and θ is the Bragg's angle.
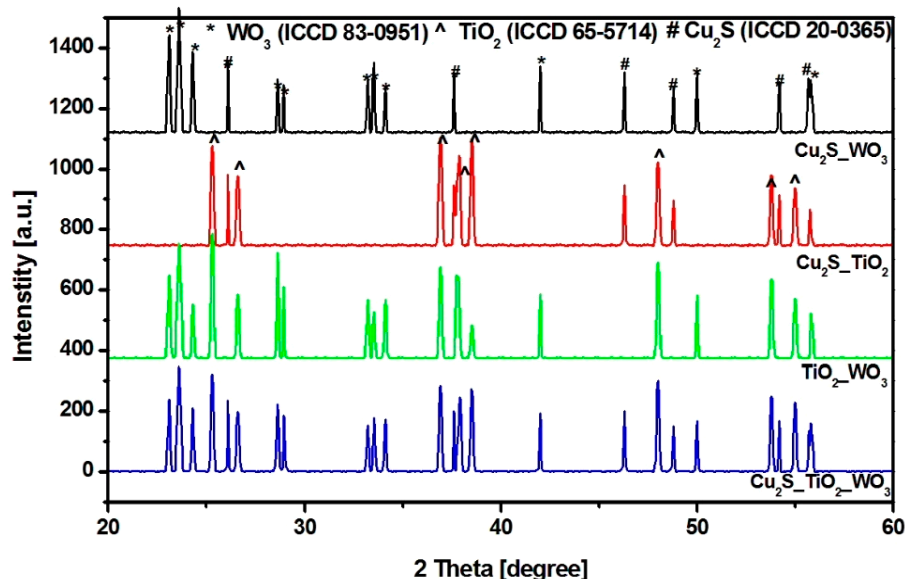

Figure 1. XRD patterns of the heterostructures.

Table 2. Average crystallite size values calculated using the Scherrer formula.

Samples Code	Crystallite Size (Å)		
	Cu_2S	TiO_2	WO_3
$Cu_2S\_TiO_2$	64	82	-
$Cu_2S\_WO_3$	79	-	103
$TiO_2\_WO_3$	-	81	96
$Cu_2S\_TiO_2\_WO_3$	65	83	97

The anatase TiO_2 structure is considered as more photosensitive compared with rutile and brookite, and suitable for photocatalytic applications. Cu_2S exhibit orthorhombic structure (djurleite, ICCD 20-0365) and the crystallite size was influenced by the insertion of metal oxides during the sol–gel procedure. The presence of TiO_2 favors the formation of smaller Cu_2S crystallites size, while WO_3 induce an increase of the copper sulfide crystallite sizes [31]. This behavior was previously presented by other researchers [32,33] in relation with similar materials. The insertion of metal oxides particles during the Cu_2S development will act as preferential nucleation sites. Using larger metal oxide crystallites size will favor the grow process, which is no longer restricted by space limitation [34]. Contrary, if the nucleation sites are based on smaller metal oxides crystallites these will also limits the Cu_2S crystallite grow rate [35]. The similar crystallites size values obtained for copper sulfide in $Cu_2S\_TiO_2$ and $Cu_2S\_TiO_2\_WO_3$ samples is an indicator of the preferential Cu_2S grow on TiO_2 during the formation of three-component heterostructure. WO_3 with monoclinic structure (ICCD 83-0951) show a similar behavior as Cu_2S, and the crystallite size decrease in the presence of TiO_2 during the sol–gel synthesis.

The morphological analyses presented in Figure 2 indicate that both mono and multi-components samples are composed on particles with irregular shape and sizes. The mono-component samples contain smaller particles, which have the tendency to form larger aggregates. The average value of mono-component particles was 0.5 μm for Cu_2S, 30 nm for TiO_2 and 0.2 μm for WO_3. The bi-component heterostructures containing Cu_2S exhibit pellets and particle-like structures closely combined in a relatively compact assembly. The $TiO_2\_WO_3$ sample has a higher homogeneity due to use of polyethylene glycol (PG) additive which favor the uniform distribution of particles and decrease the aggregates size. A similar observation was made by Dudita M. [36], showing that the dispersive component of the PG can significantly decrease the aggregates formation. However, the PG removal procedure requires higher annealing temperature, in order to avoid carbon contamination, which is not suitable for samples containing Cu_2S. Finally, the $Cu_2S\_TiO_2\_WO_3$ sample morphology indicates a uniform distribution of Cu_2S on the $TiO_2\_WO_3$ assembly.

Cu_2S TiO_2

Figure 2. *Cont.*

WO₃

Cu₂S_TiO₂
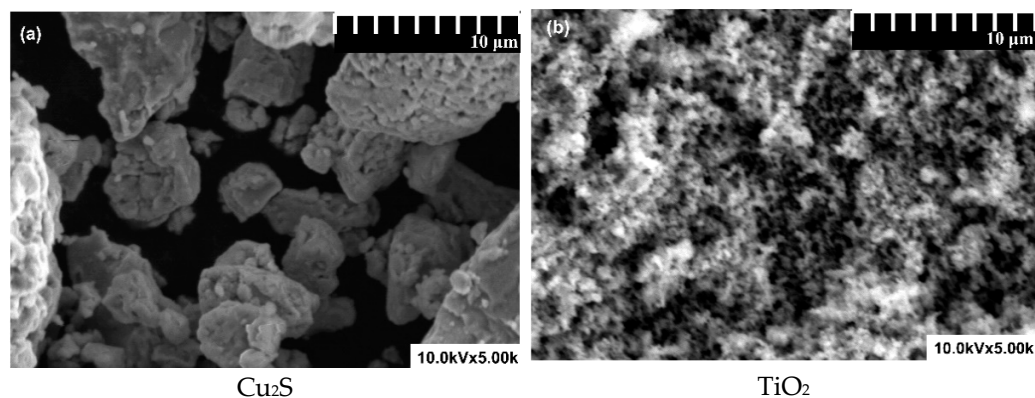
Cu₂S_WO₃

TiO₂_WO₃
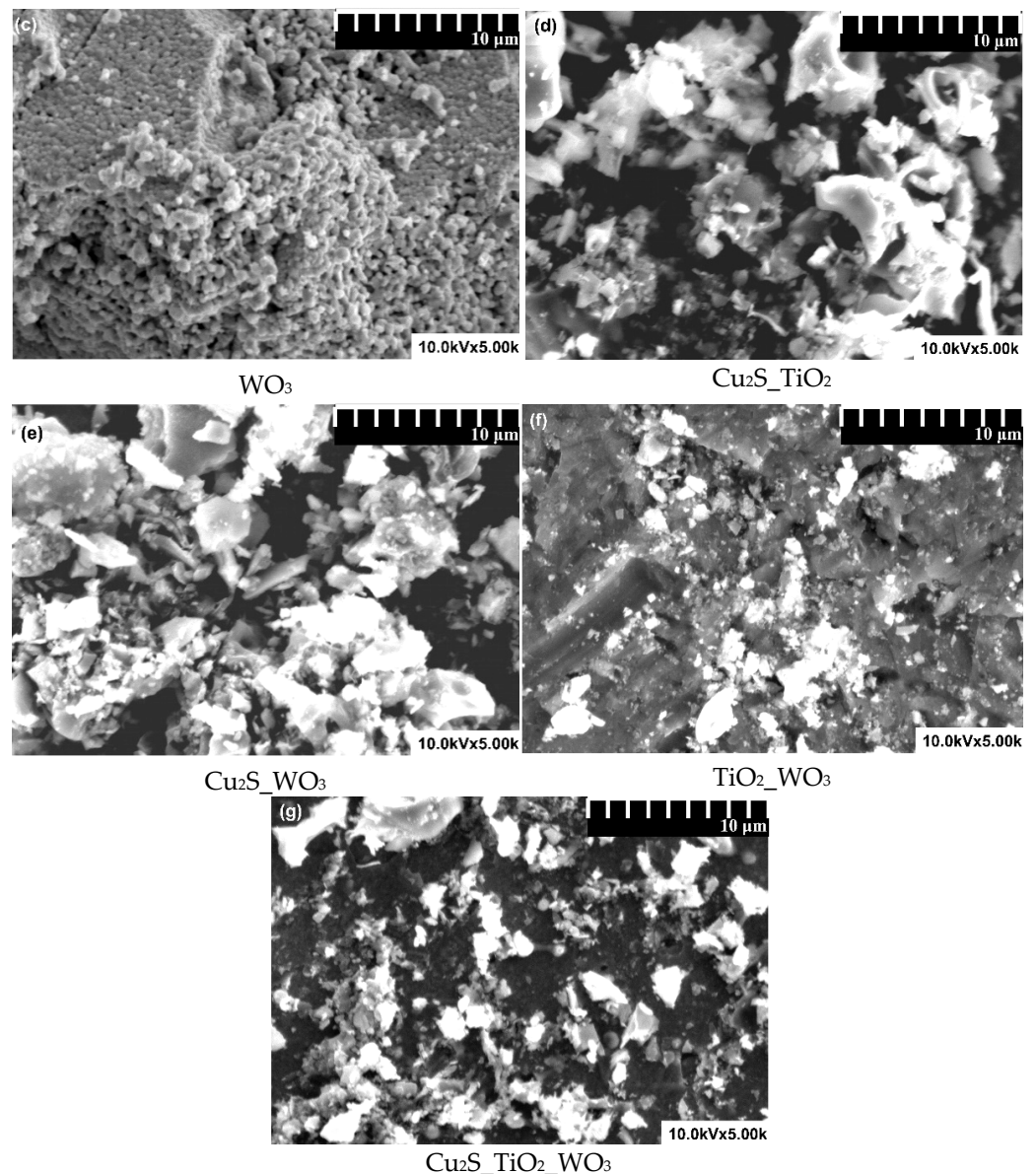
Cu₂S_TiO₂_WO₃

Figure 2. Scanning electron microscopy images of (**a**) Cu₂S, (**b**) TiO₂, (**c**) WO₃, (**d**) Cu₂S_TiO₂, (**e**).Cu₂S_WO₃, (**f**) TiO₂_WO₃, and (**g**) Cu₂S_TiO₂_WO₃.

The EDS analysis was undertaken during the morphological investigations, in order to observe the elemental surface composition and the values are presented in Table 3. The results indicate that the atomic ratio between the metals was preserved as presented in the synthesis method. Small deviations of the atomic ratio for Cu₂S_WO₃ and Cu₂S_TiO₂_WO₃ may be attributed to the non-uniform distribution at the sample surface. Additionally, the qualitative results were compared with theoretical sulfur and oxygen content, calculated based on the stoichiometric compounds identified during the X-ray diffraction investigations. The values indicate a similar tendency of sulfur deficit and oxygen excess. The results are consistent with other studies [37,38], showing that the heterostructures submitted to annealing in air may lose sulfur and develop higher oxygen content. During the annealing treatment part of the oxygen vacancy formed during the synthesis procedure will be passivated as presented in Equation (3).

$$V_O'' + \frac{1}{2}O_2 \rightarrow O_O^x + 2h^\bullet \tag{3}$$

Table 3. Average atomic composition at the heterostructure surface (EDS).

Scheme	Elemental Composition (% at)						
	Cu	**Ti**	**W**	**O**	**O_{th}** [1]	**S**	**S_{th}** [1]
$Cu_2S\_TiO_2$	23.7	22.6	-	45.4	45.2	8.3	11.8
$Cu_2S\_WO_3$	14.2	-	16.7	62.5	50.1	6.6	7.1
$TiO_2\_WO_3$	-	13.8	12.1	74.1	63.9	-	-
$Cu_2S\_TiO_2\_WO_3$	14.3	9.8	9.6	59.9	48.4	6.4	7.1

[1] Theoretic content calculated based on the stoichiometry.

3.2. Photocatalytic Properties and Mechanism

The photocatalytic activity of the mono-component and multi-component samples was tested using two irradiation scenarios: UVa (Figure 3a) and combined UVa–Vis (Figure 3b). In all cases the S-MCh herbicide concentration was 30 mg/L and photocatalyst dosage was 30 mg/50 mL. As expected, under UV irradiation the samples containing TiO_2 exhibit higher photocatalytic efficiency. The lowest photocatalytic efficiency (11.9%) was recorded for Cu_2S sample which absorb mostly in Vis spectra. However, small photocatalytic efficiency differences where observed by comparing the $Cu_2S\_TiO_2\_WO_3$ (36.6%) and $TiO_2\_WO_3$ (30.8%) heterostructures, which means that the Cu_2S contribution in UVa scenario is rather limited. This observation is valid for bi-component heterostructures containing Cu_2S coupled with a TiO_2 or WO_3, where the photocatalytic efficiency increase with few percentage than that of mono-component samples. The combined UVa–Vis scenario brings the advantage of Cu_2S component, which have a significant contribution in both bi and three-component heterostructures. The photocatalytic efficiency increase with additional 10% for $Cu_2S\_TiO_2$ and $Cu_2S\_WO_3$, comparing with UV scenario. The highest increase was observed for three-component heterostructure which reach 61.08% photocatalytic turnover rate, after 8 h of irradiation. These results are significant considering that S-MCh is considered to be a reluctant molecule towards photocatalytic decomposition due to the structural stability induced by the aromatic cycle and functional groups [39,40]. The formation of bi-products with pollutant potential cannot be excluded as partial oxidation may induce the development of carboxylic acids. Bare Cu_2S, TiO_2 and WO_3 have lower photocatalytic efficiency due to the spectral absorption limitation and faster recombination charge. The experiments made without catalyst indicate a low S-MCh decomposition rate of 1.9% under UVa irradiation and 1.7% under UVa–Vis irradiations. The S-MCh ability of self-degradation in both irradiation scenarios is negligible.
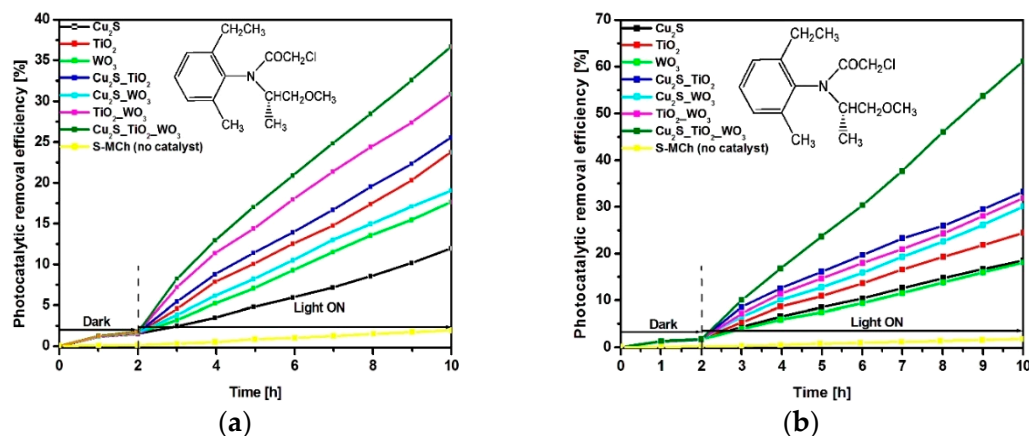
Figure 3. Photocatalytic removal efficiency under (**a**) UVa and (**b**) UVa–Vis irradiation.

The influence of photocatalysts composition and light irradiation scenario was further correlated with the kinetic investigation, based on the simplified Langmuir–Hinshelwood mathematical Equation (4) and the results are presented in Figure 4 and Table 4.
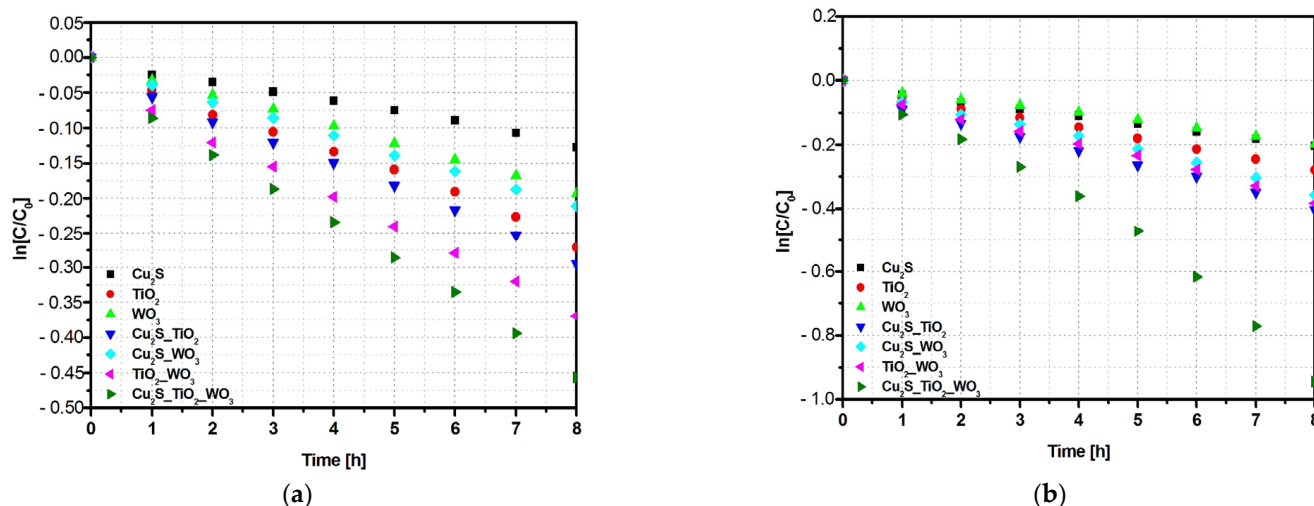
$$\ln \frac{C}{C_0} = -kt \tag{4}$$

Figure 4. Kinetic evaluation of the photocatalytic activity under (**a**) UVa and (**b**) UVa–Vis irradiation.

The kinetic data help to better understand the influence of the heterostructure composition on the photocatalytic activity. Under UVa irradiation the photocatalytic activity of $Cu_2S\_TiO_2\_WO_3$ heterostructure is 1.2x faster than $TiO_2\_WO_3$, 2.1x faster than $Cu_2S\_WO_3$, and 1.5x faster than $Cu_2S\_TiO_2$ bi-component samples. The differences increase significantly under UVa–Vis irradiation where the three-component sample photocatalytic activity is 2.5x faster than $TiO_2\_WO_3$, 2.7x faster than $Cu_2S\_WO_3$, and 2.4x faster than $Cu_2S\_TiO_2$ photocatalysts. It is worth noting that the differences between the constant rates of the bi-component heterostructures decrease in the combined irradiation scenario which confirms the contribution of Cu_2S on the overall photocatalytic efficiency [41]. The kinetic evaluation made on bare Cu_2S indicate that this component is 2x more active in UV–Vis scenario compared with UV, while TiO_2 and WO_3 exhibits small changes.

The L-H model (Equation (5)) proposed by Turchi and Ollis [42] was used to evaluate the influence of photon absorption based on both UV and UV–Vis irradiation scenarios.

$$r = -\frac{dC}{dt} = \frac{k_r K_S C}{1 + K_S C} \tag{5}$$

where C represents the S-MCh concentration (mol·L^{-1}), k_r correspond to the apparent reaction rate constant (mol·L^{-1}·min^{-1}), the apparent adsorption constant is represented by K_s (L·mol^{-1}) and the S-MCh removal rate is given by r (mol·L^{-1}·min^{-1}). It is useful to describe the apparent rate constant k (min^{-1}) as $k_r \cdot K_s$ which is a specific term for each heterostructure photocatalytic activity. The k_r depends on the light radiation parameters and allows changing the Equation (5), accordingly:

$$\frac{1}{r} = \frac{1}{k_r K_S} \cdot \frac{1}{C} + \frac{1}{k_r} \tag{6}$$

Table 4. Kinetic data corresponding to S-MCh photocatalytic removal.

Kinetic Data	Cu_2S		TiO_2		WO_3		$Cu_2S\_TiO_2$		$Cu_2S\_WO_3$		$TiO_2\_WO_3$		$Cu_2S\_TiO_2\_WO_3$	
	$K\ [S^{-1}]$	R^2	$K\ [S^{-1}]$	R^2	$K\ [S^{-1}]$	R^2	$K\ [S^{-1}]$	R^2	$K\ [S^{-1}]$	R^2	$K\ [S^{-1}]$	R^2	$K\ [S^{-1}]$	R^2
UV	0.0148	0.9958	0.0316	0.9964	0.0235	0.9992	0.0346	0.9971	0.0256	0.9984	0.0435	0.9966	0.0540	0.9977
UV–Vis	0.0243	0.9962	0.0334	0.9961	0.0237	0.9972	0.0469	0.9949	0.0419	0.9967	0.0448	0.9964	0.1140	0.9899

The results obtained based on the linear plot $1/C$ vs. $1/r$, considering the $(1/k_r)$ intercept and $(/k_r K_S)$ slope are presented in Table 5. The mathematical model indicators show that L-H fits well with the experimental photocatalytic results obtained under UV–Vis irradiation. Similar results were obtained in UV scenario for $TiO_2\_WO_3$ and $Cu_2S\_TiO_2\_WO_3$ samples. These conditions allows that the apparent reaction rates have the same order of magnitude with the apparent adsorption constant, while for the $Cu_2S\_TiO_2$ and $Cu_2S\_WO_3$ heterostructures, there is one order of magnitude difference. There are similar reports in the literature [43,44], indicating the correspondence between the light irradiation spectra and the energy bands of the heterostructure composition which contributes to the photogeneration of electrons and holes and the conversion to oxidative species.

Table 5. Heterostructures kinetic parameters for both radiation scenarios based on Equation (6).

Photocatalyst, Pollutant	$k_r \cdot 10^8$ $(Mol \cdot L^{-1} \cdot Min^{-1})$	$K_s \cdot 10^2$ $(Mol \cdot L^{-1})$
$Cu_2S\_TiO_2$, UVa	1.63	624
$Cu_2S\_TiO_2$, UVa–Vis	2.94	1682
$Cu_2S\_WO_3$, UVa	1.42	556
$Cu_2S\_WO_3$, UVa–Vis	2.98	1625
$TiO_2\_WO_3$, UVa	2.68	1044
$TiO_2\_WO_3$,UVa–Vis	2.73	1592
$Cu_2S\_TiO_2\_WO_3$, UVa	3.19	1788
$Cu_2S\_TiO_2\_WO_3$, UVa–Vis	5.26	2389

In order to evaluate the heterostructures mechanism, the components band energies (Figure 5) are necessary to provide additional information regarding the potential compatibility between them. The band energy diagram was developed based on the experimental band gap values (Figure 5b,c), corresponding to each heterostructure component and the bands energy potential were evaluated in good agreement with the methodology presented in literature [45,46]. The shift of band gap values in heterostructure may be possible due to the internal energy field. The procedure use the following Equations (7)–(10) to determine the energy band position based on the semiconductor electronegativity ($\chi_{semiconductor}$), energy of free electrons vs. hydrogen (E_e), band gap energy (E_g), absolute cationic electronegativity (χ_{cation}), and specific cationic electronegativity $\chi_{cation}(P.u.)$ where $P.u.$ represent the Pauling units.

$$E_{VB} = \chi_{semiconductor} - E_e + 0.5E_g \tag{7}$$

$$E_{CB} = E_{VB} - E_g \tag{8}$$

$$\chi_{semiconductor}(eV) = 0.45 \cdot \chi_{cation}(eV) + 3.36 \tag{9}$$

$$\chi_{cation}(eV) = \frac{\chi_{cation}(P.u) + 0.206}{0.336} \tag{10}$$

The bands energy diagram represents an S-scheme charge transfer mechanism corresponding to the heterostructures semiconductor components. Under light excitation the photogenerated electrons from the Cu_2S conduction band (-0.4 eV) will migrate to TiO_2 conduction band ($Cu_2S\_TiO_2$ and $Cu_2S\_TiO_2\_WO_3$) and further on WO_3 conduction band ($+0.4$ eV). However, the electrons from TiO_2 and WO_3 conduction bands (CB) cannot be involved in $\bullet O^-_2$ generation, and the holes from Cu_2S valence band ($+0.92$ eV) cannot produce $\bullet OH$, owing to their potential. Consequently, some of those charges which are not useful for photocatalytic reaction will recombine [47,48]. The useful electrons from the Cu_2S valence band (-0.4 eV), as well as the holes from TiO_2 ($+2.9$ eV) and WO_3 ($+3.1$ eV) valence bands, have a stronger redox ability and are efficiently separated by the electric field in the charged space region. Under the combined drift and diffusion effect, the photogenerated charges will migrate through the heterostructure components, [49,50]. The higher photocatalytic efficiency exhibited by $Cu_2S\_TiO_2\_WO_3$ is explained by the synergic

activity of a dual S-scheme mechanism between the Cu_2S/TiO_2 and TiO_2/WO_3, respectively. The band gap values of each components shift, allowing the formation of a collective heterostructure band gap. The Tauc plot presented in Figure 5e indicate a band gap value of 1.45 eV for $Cu_2S\_TiO_2\_WO_3$ heterostructure, confirming the absorbance in both UV and Vis light spectra. Therefore, the development of S-scheme heterostructure systems could efficiently promote the photoexcited charge carriers separation which determine the increase of (super)oxidative species concentration acting on S-MCh photocatalytic removal.
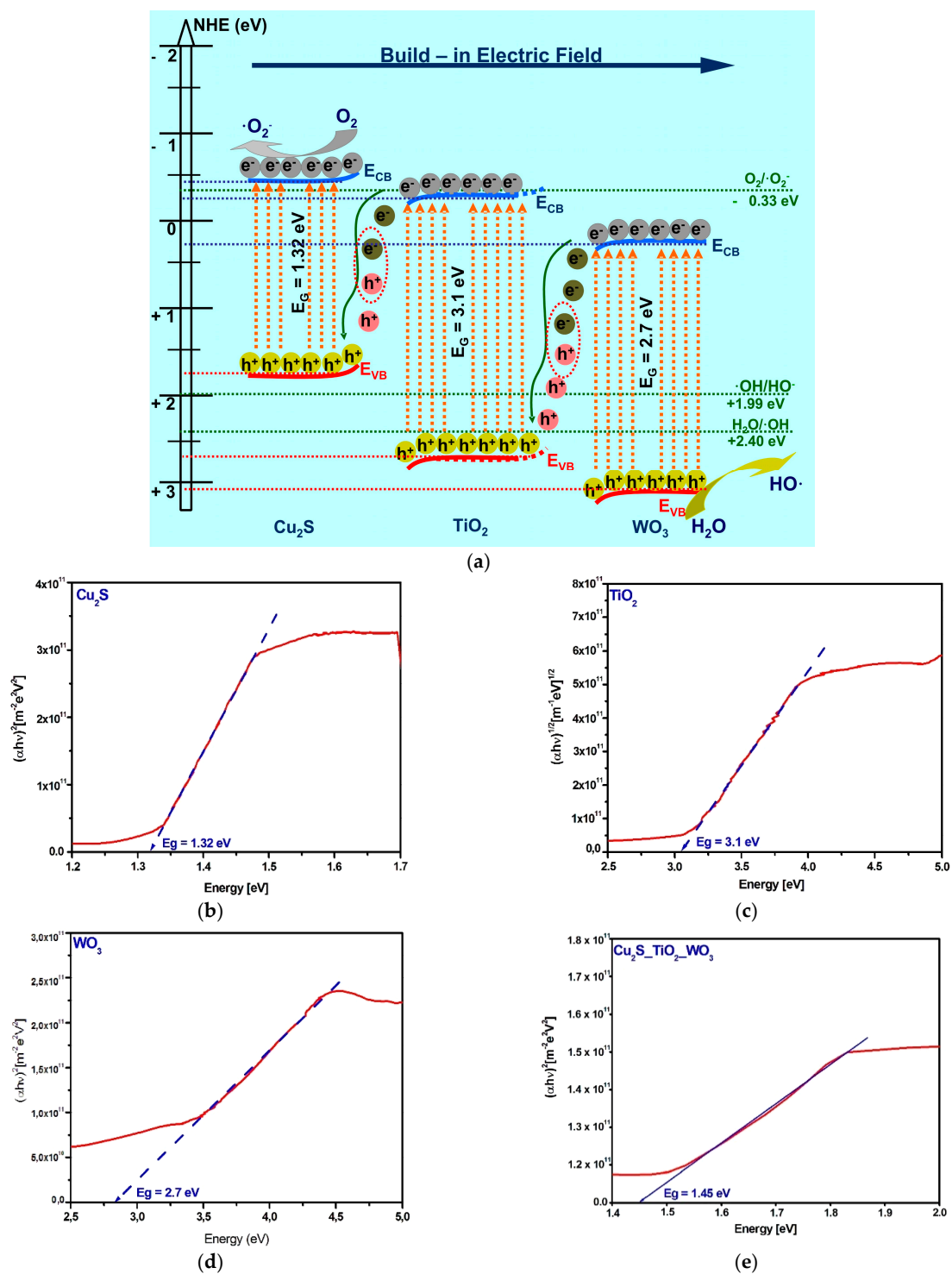

Figure 5. (**a**) Band energy diagram of the S-scheme heterostructure and the corresponding (**b**) Cu_2S, (**c**) TiO_2, (**d**) WO_3, and (**e**) $Cu_2S\_TiO_2\_WO_3$ band gaps.

4. Conclusions

A dual $Cu_2S\_TiO_2\_WO_3$ S-scheme heterostructure was prepared by sol-gel technique and the photocatalytic properties where tested and compared with other samples. The heterostructure is composed on orthorhombic Cu_2S, anatase TiO_2 and monoclinic WO_3, with crystallite sizes varying from 65.2 Å for Cu_2S to 97.1 Å for WO_3. The heterostructure exhibit a dense morphology with pellets and particle-like morphology closely combined, in a relatively compact assembly. The surface elemental composition indicate that the heterostructure maintain a similar atomic ratio as established during the synthesis, with a slight sulfur deficit and oxygen excess due to the annealing treatments.

The photocatalytic activity toward S-MCh herbicide removal was evaluated using UVa and UVa–Vis irradiation scenarios. The results indicate a superior photocatalytic activity of $Cu_2S\_TiO_2\_WO_3$, compared with $Cu_2S\_TiO_2$, $Cu_2S\_WO_3$, $TiO_2\_WO_3$ or bare components. Under UVa–Vis irradiation the $Cu_2S\_TiO_2\_WO_3$ heterostructure reach 61% photocatalytic efficiency with a constant rate of 0.1140 s^{-1} ($2.5\times$ faster than $TiO_2\_WO_3$ and $2.7\times$ faster than $Cu_2S\_WO_3$). The higher photocatalytic activity of $Cu_2S\_TiO_2\_WO_3$ sample was attributed to the formation of dual S-scheme mechanism, allowing the increase of photogenerated charge carrier concentration, efficient charge separation and migration.

Future studies will be dedicated to the improvement of the photocatalytic efficiency using two approaches: (1) the optimization of heterostructure components ratio in order to increase the concentration of oxidative species, and (2) the replacement of one components in order to maximize the photons conversion during the photocatalytic activity. Both ways will preserve the S-mechanisms which seems to be the most favorable for resilient organic pollutants molecules. Additionally, HPLC studies will be included to investigate the formation of potential pollutant bi-products during the photocatalytic activity.

Author Contributions: Conceptualization, A.E.; methodology, A.E.; validation, L.I.; formal analysis, L.I.; investigation, A.E.; resources, L.I.; data curation, L.I.; writing—original draft preparation, A.E.; writing—review and editing, A.E.; visualization, L.I.; supervision, L.I.; project administration, A.E.; funding acquisition, A.E. All authors have read and agreed to the published version of the manuscript.

Institutional Review Board Statement: Not applicable.

Informed Consent Statement: Not applicable.

Data Availability Statement: Data presented in this study are available by requesting from the corresponding author.

Conflicts of Interest: The authors declare no conflict of interest. The funders had no role in the design of the study; in the collection, analyses, or interpretation of data; in the writing of the manuscript, or in the decision to publish the results.

References

1. Matheus, M.C.; Lourenço, G.R.; Solano, B.A.; Dezotti, M.W.C.; Bassin, J.P. Assessing the impact of hydraulic conditions and absence of pretreatment on the treatability of pesticide formulation plant wastewater in a moving bed biofilm reactor. *J. Water Proc. Eng.* **2020**, *36*, 101243. [CrossRef]
2. Alistea, M.; Garridoa, I.; Floresa, P.; Hellína, P.; Velab, N.; Navarroc, S.; Fenoll, J. Reclamation of agro-wastewater polluted with thirteen pesticides by solar photocatalysis to reuse in irrigation of greenhouse lettice grown. *J. Environ. Manag.* **2020**, *266*, 110565. [CrossRef] [PubMed]
3. Xiao, Z.; Wang, L.; Zhang, Y.; Wang, Y.; Saleha, A.S.M.; Zhu, M.; Gao, Y.; Xu, C.; Hassana, M.E.; Yang, Q.; et al. Synthesis and characterization of a novel rice bran protein-cerium complex for the removal of organophosphorus pesticide residues from wastewater. *Food Chem.* **2020**, *320*, 126604.
4. Fang, H.; Zhang, H.; Han, L.; Mei, J.; Ge, Q.; Long, Z.; Yu, Y. Exploring bacterial communities and biodegradation genes in activated sludge from pesticide wastewater treatment plants via metagenomic analysis. *Environ. Pollut.* **2018**, *243*, 1206–1216. [CrossRef]
5. Sharma, L.; Kakkar, R. Magnetically retrievable one-pot fabrication of mesoporous magnesium ferrite ($MgFe_2O_4$) for the remediation of chlorpyrifos and real pesticide wastewater. *J. Environ. Chem. Eng.* **2018**, *6*, 6891–6903. [CrossRef]

6. Ghodsi, J.; Rafati, A.A. A voltammetric sensor for diazinon pesticide based on electrode modified with TiO_2 nanoparticles covered multi walled carbon nanotube nanocomposite. *J. Electroanal. Chem.* **2017**, *807*, 1–9. [CrossRef]

7. Fernández-Domene, R.M.; Sánchez-Tovar, R.; Lucas-Granados, B.; Muñoz-Portero, M.J.; García-Antón, J. Elimination of pesticide atrazine by photoelectrocatalysis using a photoanode based on WO_3 nanosheets. *Chem. Eng. J.* **2018**, *350*, 1114–1124. [CrossRef]

8. Huang, X.; Wang, L.; Sun, Y.; Meng, F.; Liu, J. Quantitative analysis of pesticide residue based on the dynamic response of a single SnO_2 gas sensor. *Sens. Acuat. B* **2004**, *99*, 330–335. [CrossRef]

9. Honarnezhad, R.; Fathinia, M.; Khataee, A. Mechanical production and sonocatalytic application of Cu_2S nanoparticles for degradation of isopropylxanthic acid: Kinetic modeling via white and black box methods. *J. Mol. Liq.* **2019**, *287*, 110899. [CrossRef]

10. Tunesi, M.M.; Kalwar, N.; Abbas, M.W.; Karakus, S.; Soomro, R.A.; Kilislioglu, A.; Abro, M.I.; Hallam, K.R. Functionalised CuO nanostructures for the detection of organophosphorus pesticides: A non-enzymatic inhibition approach coupled with nano-scale electrode engineering to improve electrode sensitivity. *Sens. Acuat. B* **2018**, *260*, 480–489. [CrossRef]

11. Ramu, A.G.; Arun Kumari, M.L.; Elshikh, M.S.; Alkhamis, H.H.; Alrefaei, A.F.; Choi, D. A facile and green synthesis of CuO/NiO nanoparticles and their removal activity of toxic nitro compounds in aqueous medium. *Chemosphere* **2020**, *271*, 129475. [CrossRef]

12. Zhu, D.; Zhou, Q. Action and mechanism of semiconductor photocatalysis on degradation of organic pollutants in water treatment: A review. *Environ. Nanotech. Monit. Manag.* **2019**, *12*, 100255. [CrossRef]

13. Mouchaal, Y.; Enesca, A.; Mihoreanu, C.; Khelil, A.; Duta, A. Tuning the opto-electrical 350 properties of SnO_2 thin films by Ag^{+1} and In^{+3} co-doping. *Mater. Sci. Eng. B Adv.* **2015**, *199*, 22–29. [CrossRef]

14. Nicholls, T.P.; Bissember, A.C. Developments in visible-light-mediated copper photocatalysis. *Tetrahedron Lett.* **2019**, *60*, 150883. [CrossRef]

15. Sheng, Y.; Wei, Z.; Miao, H.; Yao, W.; Li, H.; Zhu, Y. Enhanced organic pollutant photodegradation via adsorption/photocatalysis synergy using a 3D g-C_3N_4/TiO_2 free-separation photocatalyst. *Chem. Eng. J.* **2019**, *370*, 287–294. [CrossRef]

16. Meng, S.; Zhang, J.; Chen, S.; Zhang, S.; Huang, W. Perspective on construction of heterojunction photocatalysts and the complete utilization of photogenerated charge carriers. *Appl. Surf. Sci.* **2019**, *476*, 982–992. [CrossRef]

17. Deng, H.; Fei, X.; Yang, Y.; Fan, J.; Yu, J.; Cheng, B.; Zhang, L. S-scheme heterojunction based on p-type $ZnMn_2O_4$ and n-type ZnO with improved photocatalytic CO2 reduction activity. *Chem. Eng. J.* **2021**, *409*, 127377. [CrossRef]

18. Li, J.; Li, M.; Jin, Z. 0D CdxZn1-xS and amorphous Co9S8 formed S-scheme heterojunction boosting photocatalytic hydrogen evolution. *Mol. Catal.* **2021**, *501*, 111378. [CrossRef]

19. Pham, T.T.; Shin, E.W. Thermal formation effect of g-C_3N_4 structure on the visible light driven photocatalysis of g-C_3N_4/$NiTiO_3$ Z-scheme composite photocatalysts. *Appl. Surf. Sci.* **2018**, *447*, 757–766. [CrossRef]

20. Chang, N.; Chen, Y.R.; Xie, F.; Liu, Y.P.; Wang, H.T. A promising Z-scheme heterojunction via loading Ag/AgCl into porous Co_3O_4 derived from ZIF-67 for visible light driven photocatalysis. *Micropor. Mesopor. Mat.* **2020**, *307*, 110530. [CrossRef]

21. Dursun, S.; Koyuncu, S.N.; Kaya, I.C.; Kaya, G.G.; Kalem, V.; Akyildiz, H. Production of CuO–WO_3 hybrids and their dye removal capacity/performance from wastewater by adsorption/photocatalysis. *J. Water Proc. Eng.* **2020**, *36*, 101390. [CrossRef]

22. Ojha, D.P.; Karki, H.P.; Song, J.H.; Kim, H.J. Amine-assisted synthesis of $FeWO_4$ nanorodg-C3N4 for enhanced visible light-driven Z-scheme photocatalysis. *Compos. Part B Eng.* **2019**, *160*, 277–284. [CrossRef]

23. Li, Y.; He, R.; Han, P.; Hou, B.; Peng, S.; Ouyang, C. A new concept: Volume photocatalysis for efficient H_2 generation using low polymeric carbon nitride as an example. *Appl. Cat. B Environ.* **2020**, *279*, 119379. [CrossRef]

24. Chen, H.J.; Yang, Y.L.; Hong, M.; Chen, J.G.; Suo, G.Q.; Hou, X.J.; Feng, L.; Chen, Z.G. Separable and recyclable meso-carbon@TiO_2/carbon fiber composites for visible-light photocatalysis and photoelectrocatalysis. *Sustain. Mater. Technol.* **2019**, *21*, e00105. [CrossRef]

25. Li, X.; Hu, T.; Zhang, J.; Dai, K.; Liang, C. Novel 2D $SnNb_2O_6$/Ag_3VO_4 S-scheme heterojunction with enhanced visible-light photocatalytic activity. *Ceram. Int.* **2021**, *47*, 7169–7176. [CrossRef]

26. Wang, R.; Shen, J.; Zhang, W.; Liu, Q.; Zhang, M.; Tang, H. Build-in electric field induced step-scheme TiO_2/$W_{18}O_{49}$ heterojunction for enhanced photocatalytic activity under visible-light irradiation. *Ceram. Int.* **2020**, *46*, 23–30. [CrossRef]

27. Hu, X.; Wang, G.; Wang, J.; Hu, Z.; Su, Y. Step-scheme NiO/BiOI heterojunction photocatalyst for rhodamine photodegradation. *Appl. Surf. Sci.* **2020**, *511*, 145499. [CrossRef]

28. Xu, A.J.; Tu, W.; Shen, S.; Lin, Z.; Gao, N.; Zhong, W. $BiVO_4$@MoS_2 core-shell heterojunction with improved photocatalytic activity for discoloration of Rhodamine B. *Appl. Surf. Sci.* **2020**, *528*, 146949. [CrossRef]

29. Pei, C.Y.; Chen, Y.G.; Wang, L.; Chen, W.; Huang, G.B. Step-scheme WO_3/$CdIn_2S_4$ hybrid system with high visible light activity for tetracycline hydrochloride photodegradation. *Appl. Surf. Sci.* **2021**, *535*, 147682. [CrossRef]

30. Wei, J.; Chen, Y.; Zhang, H.; Zhuang, Z.; Yu, Y. Hierarchically porous S-scheme CdS/UiO-66 photocatalyst for efficient 4-nitroaniline reduction. *Chin. J. Catal.* **2021**, *42*, 78–86. [CrossRef]

31. Guan, R.; Zhai, H.; Li, J.; Qi, Y.; Li, M.; Song, M.; Zhao, Z.; Zhang, J.; Wang, D.; Tan, H. Reduced mesoporous TiO_2 with Cu_2S heterojunction and enhanced hydrogen production without noble metal cocatalyst. *Appl. Surf. Sci.* **2019**, *507*, 144772. [CrossRef]

32. Singh, S.V.; Sharma, A.; Biring, S.; Pal, B.N. Solution processed Cu_2S/TiO_2 heterojunction for visible-near infrared photodetector. *Thin Solid Films* **2020**, *710*, 138275. [CrossRef]

33. Baviskar, V.; Salunkhe, D.; Tarkas, H.; Wagh, R.; Baviskar, P.; Patil, R. Sensitization of TiO_2 by chemically deposited Cu_2S for solar cell: Effect of deposition time on photoelectrochemical performance. *Optik* **2020**, *207*, 163890. [CrossRef]

34. Rao, V.N.; Reddy, N.L.; Kumari, M.M.; Ravi, P.; Sathish, M.; Kuruvilla, K.M.; Preethi, V.; Reddy, K.R.; Shettie, N.P.; Aminabhavi, T.M.; et al. Photocatalytic recovery of H$_2$ from H$_2$S containing wastewater: Surface and interface control of photo-excitons in Cu$_2$S@TiO$_2$ core-shell nanostructures. *Appl. Catal. B Environ.* **2019**, *254*, 174–185.

35. Baneto, M.; Enesca, A.; Mihoreanu, C.; Lare, Y.; Jondo, K.; Napo, K.; Duta, A. Effects of the growth temperature on the properties of spray deposited CuInS$_2$ thin films for photovoltaic applications. *Ceram. Int.* **2015**, *41*, 4742–4749. [CrossRef]

36. Dudita, M.; Bogatu, C.; Enesca, A.; Duta, A. The influence of the additives composition and concentration on the properties of SnO$_x$ thin films used in photocatalysis. *Mater. Lett.* **2011**, *65*, 2185–2189. [CrossRef]

37. Zhang, L.; Zhao, Y.; Zhong, L.; Wang, Y.; Chai, S.; Yang, T.; Han, X. Cu$_2$S-Cu-TiO$_2$ mesoporous carbon composites for the degradation of high concentration of methyl orange under visible light. *Appl. Surf. Sci.* **2017**, *422*, 1093–1101. [CrossRef]

38. Tang, L.; Deng, Y.; Zeng, G.; Hu, W.; Wang, J.; Zhou, Y.; Wang, J.; Tang, J.; Fang, W. CdS/Cu$_2$S co-sensitized TiO$_2$ branched nanorod arrays of enhanced photoelectrochemical properties by forming nanoscale heterostructure. *J. Alloy. Compound.* **2016**, *662*, 516–527. [CrossRef]

39. Marín-Benito, J.M.; Herrero-Hernández, E.; Ordaxa, J.M.; Sánchez-Martín, M.J.; Rodríguez-Cruz, M.S. The role of two organic amendments to modify the environmental fate of S-metolachlor in agricultural soils. *Environ. Res.* **2021**, *195*, 110871. [CrossRef] [PubMed]

40. Yang, L.; Ivantsova, E.; Souders, C.L., II; Martyniuk, C.J. The agrochemical S-metolachlor disrupts molecular mediators and morphology of the swim bladder: Implications for locomotor activity in zebrafish (*Danio rerio*). *Ecotox. Environ. Safe* **2021**, *208*, 111641. [CrossRef]

41. Sithole, R.K.; Machogo, L.F.E.; Moloto, M.J.; Gqoba, S.S.; Mubiayi, K.P.; Wyk, J.V.; Moloto, N. One-step synthesis of Cu$_3$N, Cu$_2$S and Cu$_9$S$_5$ and photocatalytic degradation of methyl orange and methylene blue. *J. Photochem. Photobiol. A Chem.* **2020**, *397*, 112577. [CrossRef]

42. Turchi, C.S.; Ollis, D.F. Photocatalytic degradation of organic water contaminants: Mechanisms involving hydroxyl radical attack. *J. Catal.* **1990**, *122*, 178–192. [CrossRef]

43. Xu, F.; Costa, M.F.; Sun, S.; Teixeira, V.; Wang, Y.; Bian, F.; Wang, H.; Cui, H. Structure Optimization on the Photoelectric and Photocatalytic Properties of Cu$_2$S and ZnO Complex Films. *Mater. Today Proc.* **2015**, *2*, 253–260. [CrossRef]

44. Herrmann, J.M.; Guillard, C.; Pichat, P. Heterogeneous photocatalysis: An emerging technology for water treatment. *Catal. Today* **1993**, *17*, 7–20. [CrossRef]

45. Gao, C.; Li, J.; Shan, Z.; Huang, F.; Shen, H. Preparation and visible-light photocatalytic activity of In$_2$S$_3$/TiO$_2$ composite. *Mater. Chem. Phys.* **2010**, *122*, 183–187. [CrossRef]

46. Mise, T.; Nakada, T. Low temperature growth and properties of Cu–In–Te based 433 thin films for narrow bandgap solar cells. *Thin Solid Films* **2010**, *518*, 5604–5609. [CrossRef]

47. Liu, Y.; Gong, Z.; Lv, H.; Ren, H.; Xing, X. Rational design of Au decorated Mn$_{0.5}$Cd$_{0.5}$S/WO$_3$ step-scheme heterostructure with multichannel charge transfer and efficient H$_2$ generation. *Appl. Surf. Sci.* **2020**, *526*, 146734. [CrossRef]

48. Jia, X.; Han, Q.; Liu, H.; Li, S.; Bi, H. A dual strategy to construct flowerlike S-scheme BiOBr/BiOAc1$-$xBrx heterojunction with enhanced visible-light photocatalytic activity. *Chem. Eng. J.* **2020**, *399*, 125701. [CrossRef]

49. He, R.; Liu, H.; Liu, H.; Xu, D.; Zhang, L. S-scheme photocatalyst Bi$_2$O$_3$/TiO$_2$ nanofiber with improved photocatalytic performance. *J. Mater. Sci. Technol.* **2020**, *52*, 145–151.

50. Enesca, A.; Isac, L.; Duta, A. Charge carriers injection in tandem semiconductors for dyes mineralization. *Appl. Catal. B.* **2015**, *162*, 352–363. [CrossRef]